

Prediction of Residual Deformation and Stress of Laser Powder Bed Fusion Manufactured Ti-6Al-4V Lattice Structures Based on Inherent Strain Method

Mingju Gan^a, Qi Wu^{a*} , Lianchun Long^a

^aBeijing University of Technology, Faculty of Materials and Manufacturing, 100124, Beijing, China.

Received: December 03, 2022; Revised: February 25, 2023; Accepted: March 01, 2023

The development of additive manufacturing (AM) technology provides higher feasibility for designing and manufacturing lattice structures. However, the manufacturing process usually generates residual deformation and stress, and even produces cracking, thus affecting the performance of the parts. This work establishes a simulation model of the Ti-6Al-4V lattice structures during laser powder bed fusion (LPBF) based on the inherent strain method. Effects of geometric lattice parameters (inclination angle, rod diameter, rod length) on the residual deformation and stress are analyzed. Based on the simulation results, measures for improving the quality of the lattice structures are proposed. The proposed model and simulation results can provide theoretical references for designing and manufacturing the lattice structures during practical engineering applications of LPBF.

Keywords: LPBF, Inherent strain method, Lattice structures, Residual deformation, Ti-6Al-4V.

1. Introduction

Lattice structures have become promising new structural materials for current industrial applications because of their lightweight, high specific strength, and ductility¹⁻³. Traditional manufacturing methods make it difficult to shape complex and delicate lattice structures. In contrast, the rapidly developing additive manufacturing (AM) technology in recent years has the technological characteristics of laminated manufacturing. It has opened up new ideas and feasibility for manufacturing lattice structures⁴⁻⁶.

Metal lattice structures prepared by AM technology have excellent mechanical properties. However, due to its rapid solidification characteristics, there are large residual stresses in the sample and poor forming accuracy, resulting in damage to its mechanical properties. Zhang et al.⁷ studied the manufacturability of Ti-6Al-4V lattice struts by selective electron beam manufacturing (SEBM). It is shown that the alloy roughness decreases as the lattice struts diameter increases, and the forming angle is the most important factor affecting the quality of lattice forming. Kadirgama et al.⁸ investigated the properties of Ti6Al4V lattice structures fabricated via selective laser melting (SLM). It was found that the porosity increased, the dimensional accuracy, Young's modulus, and yield strength decreased sharply, while the roughness went up sharply, and the single cell size and strut size had no significant effect on them. The dimensional accuracy of the cylindrical strut is lower than that of the hexagonal strut. Xiao et al.⁹ used SLM technique combined with topology optimization to design and fabricate three types of lattice structures. The FCC and VC lattice structures have better mechanical properties than the ECC lattice structure. Although the ECC structure has the highest residual stress value it also has the highest energy absorption efficiency. Overall,

the lattice structures' topology and geometric factors have an impact on the manufacturability of AM lattice structures.

Laser powder bed melting (LPBF) is one of the most widely used AM technologies, including popular metal printing technologies, such as SLM and direct metal laser sintering (DMLS). The metal parts are constructed layer by layer from the bottom of the powder bed upwards. Generally, the metal powder is selectively melted by an intense laser beam, and the molten material becomes solid through rapid cooling and solidification¹⁰⁻¹³. However, the LPBF technique also has some deficiencies. The excessive temperature gradient will lead to high residual stress and deformation of materials, and components are prone to warping deformation and cracks¹⁴⁻¹⁶. To reduce the hazards caused by residual deformation and stress during AM, numerical simulation can be used to predict in advance. Based on the predicted and optimized process parameters, the printing success rate and quality are in a good chance of promotion.

Nowadays, the simulated results of thermo-mechanical coupling models are in good agreement with experimental observations when actual laser scanning paths and printing parameters are considered. Nevertheless, the simulation processes are characterized by long computational time and high consumption of computational resources. Especially for the lattice structures with more detailed features, mesh generation is challenging. These problems make it almost impossible to realize the thermo-mechanical coupling simulation method in the lattice structures^{17,18}. In comparison, the inherent strain method only focuses on the inherent strain in and around the deformation area. The deformation results can be obtained after a single elastic calculation, significantly reducing the calculation time and cost.

Many research efforts have focused on developing effective models to predict residual stresses and deformations

*e-mail: qiwu@bjut.edu.cn

in AM metal to ensure computational accuracy and efficiency. The Japanese scholar Ueda et al.¹⁹ proposed the inherent strain method in 1975, which was initially applied to predicting deformation in welding processes. Deng et al.²⁰ proposed the inherent deformation method based on the theory of the inherent strain method. It realizes the converting of strain into deformations, simplifying the calculation process. Keller and Ploshikhin²¹ used the inherent strain finite element method to simulate deformed parts during the SLM process, and deformation variation of the parts was obtained. However, no detailed theory or method was given to determine the inherent strain in the AM construction. Siewert et al.²² proposed a mechanical layer equivalence method that uses the inherent strain vector as input to the part-scale model. Based on two benchmark double cantilever beams, the inherent strain values were obtained experimentally. The simulated residual deformation and stress of the two cross-cantilever beams made of the Ti6Al4V alloy are compared with the experimental results, and reasonable consistency is found. Setien et al.²³ proposed an empirical method to determine the inherent strain values based on the experimental measurement of residual deformation. An improved inherent strain model was proposed to extract the inherent strain from small-scale thermo-dynamic coupling simulations. Then the residual deformation of the lens and L-PBF components was predicted. Liang et al.²⁴⁻²⁶ modified the inherent strain method according to the characteristics of the AM process to predict the deformation of additively manufactured parts. The predicted results were compared with the experiments and were in good agreement. Chen et al.²⁷ proposed a multiscale process modeling framework for efficiently and accurately simulating residual distortion and stress at the part-scale for the DMLS process. The effectiveness is verified by simulating double cantilever beams and typical components with different wall thicknesses and comparing them with experimental measurement results. Dong et al.²⁸ proposed a new MIS method to improve the simulation accuracy of residual stress without degrading the residual deformation prediction. The experimental and numerical simulation results show that it can well predict the residual stress and deformation of L-PBF metal parts.

Most existing studies investigate the influence of process parameters on the residual deformation and stress, and few summarize the influence of geometric factors on the residual deformation and stress of the components themselves. In this work, we adopt the inherent strain method to simulate both lattice cell and multilayer structures' forming processes. Then analyze the residual deformation and stress distribution trends. Under the constraints of the unsupported forming process of the additive manufactured lattice structures, the influence of geometric parameters (inclination, diameter, and length of the rod cores) on the residual deformation and stress are further discussed. It provides a theoretical reference for designing and manufacturing lattice structures in practical engineering applications.

2. Model Description

Based on the inherent strain method, this paper mainly divides into the following steps to predict the residual stress and deformation generated by LPBF manufacturing lattice

structures: 1) Establish the calibration model of the melt pool size. The simulated melt pool size was compared with the experiments in the literature. The anisotropic heat conduction enhancement coefficient is determined to improve the accuracy of the heat source model; 2) The calibration results are used as the conditions for the LPBF thermo-mechanical coupling model to extract the inherent strain; 3) The results of the inherent strain vector are loaded into the lattice structures as the coefficient of thermal expansion to predict the residual deformation and stress. The calculation process is shown in Figure 1.

2.1. Thermo-mechanical coupling theory

LPBF forming is characterized by a significant nonlinear transient heat transfer process. The influence of molten pool flow on temperature field distribution and the molten pool size is not considered in LPBF, forming a finite element model. To mitigate this effect, the anisotropic thermal conductivity enhancement coefficient can be set²⁹. The modified heat transfer equation is shown in Equation 1:

$$\rho c \frac{\partial T}{\partial t} = \frac{\partial}{\partial x} \left(\omega_x k_x \frac{\partial T}{\partial x} \right) + \frac{\partial}{\partial y} \left(\omega_y k_y \frac{\partial T}{\partial y} \right) + \frac{\partial}{\partial z} \left(\omega_z k_z \frac{\partial T}{\partial z} \right) + q \quad (1)$$

Where ρ is the material density; c is the specific heat capacity; t is the time; T is the temperature; k_x, k_y, k_z are the thermal conductivity in different directions; $\omega_x, \omega_y, \omega_z$ is the thermal conductivity enhancement coefficients in the x, y, z directions, respectively.

The power density of the mobile laser heat source used in this simulation conforms to a Gaussian distribution, which is expressed as a function of Equation 2:

$$q = \frac{2AP}{\pi r_0^2} \exp \left(-2 \frac{r^2}{r_0^2} \right) \quad (2)$$

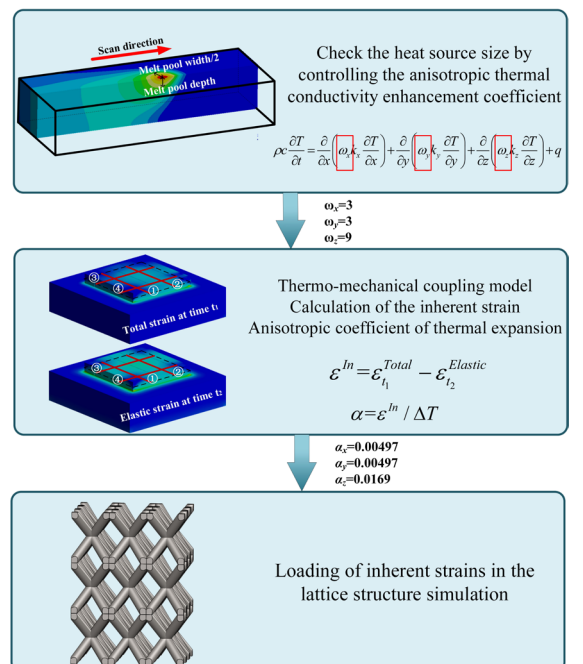


Figure 1. Schematic diagram of the simulation process.

Where q is the laser power density; P is the laser power; r_0 is the spot radius; r is the distance from a point in space to the center of the spot; A is the absorption rate of Ti-6Al-4V metal powder to the laser at that wavelength, which is taken as 0.42³⁰.

The initial temperature of its heat source model is the initial condition:

$$T|_{t=0} = T_0(x, y, z, t) \quad (3)$$

Its boundary conditions consist of convective heat transfer and radiative heat transfer, and the heat source boundary conditions are:

$$k_x \frac{\partial T}{\partial x} \eta_x + k_y \frac{\partial T}{\partial y} \eta_y + k_z \frac{\partial T}{\partial z} \eta_z = \varepsilon \sigma (T^4 - T_0^4) + h(T - T_0) \quad (4)$$

Where: T_0 is the ambient temperature set to 298.15K; η_x, η_y, η_z are the cosines of the direction normal to the outer boundary; ε_0 is the thermal radiation coefficient; σ is the Stefan-Boltzmann constant, taking the value of $5.67 \times 10^{-8} \text{W}/(\text{m}^2 \cdot \text{K}^4)$; h is the convective heat transfer coefficient.

The metal powder used in this study is Ti-6Al-4V alloy, and the two materials, metal powder and metal solid, are defined in the analysis process. The main difference between the two is the significant difference in the thermal conductivity of the materials. Figure 2 shows the thermo-physical parameters of Ti-6Al-4V used in the study^{31,32}. The melting point of Ti-6Al-4V material was taken as 1923.15 K. The α to β phase temperature was 1268.15 K. The initial powder porosity was 0.48.

The established finite element model for melt pool size calibration is shown in Figure 3. The model's dimensions are 0.5mm × 1.0mm × 0.2mm, and the material is Ti-6Al-4V. The process parameters used to simulate LPBF are consistent with the literature³¹ experiments, as shown in Table 1. The size

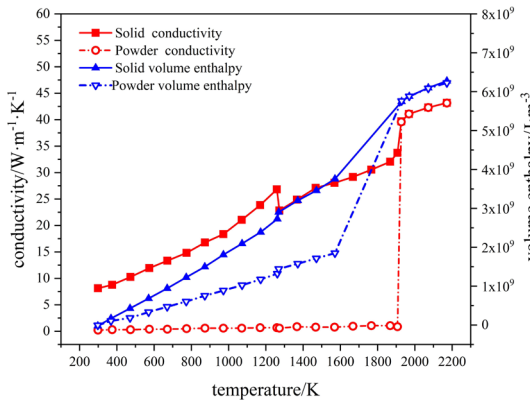


Figure 2. Thermal physical parameters of Ti-6Al-4V^{31,32}.

of the heat source is calibrated by comparing the simulated temperature fields with that of the actual forming.

For the stress calculation, the material deformation is assumed to satisfy the von Mises yield criterion and obeys the flow and bilinear hardening criterion. After obtaining the temperature field through thermal simulation, the calculated temperature field results are introduced into the mechanical model to analyze the stress field. The relationship between stress and strain is:

$$\sigma = D \varepsilon^e \quad (5)$$

$$\varepsilon^e = \varepsilon \times \varepsilon^{th} \quad (6)$$

Where: σ is the stress vector; D is the elastic matrix; ε^e is the elastic strain vector; ε is the total strain vector; ε^{th} is the thermal strain vector. Fix the bottom of the base plate in the simulation process to limit the movement and deformation of the bottom.

The specific values of the thermal physical parameters for the stress field analysis^{33,34} are shown in Table 2. The values of the material properties between adjacent temperature points are calculated by linear interpolation.

2.2. Inherent strain theory

In the process of LPBF, the molten part of the powder produces thermal contraction and expansion in the solidification area due to heat transfer. If the stress at this point exceeds the material's elastic limit, the plastic strain will be generated, resulting in plastic deformation. The sum of the plastic strains generated when the temperature increases and decreases are the residual plastic strain, namely the inherent strain. In the process of metal powder material from melting to cooling solidification, the total strain is equal to the sum of elastic strain, plastic strain, thermal strain, and the corresponding change.

$$\varepsilon = \varepsilon^e + \varepsilon^T + \varepsilon^P + \varepsilon \quad (7)$$

Where: ε^e is the elastic strain; ε^T is the thermal strain; ε^P is the plastic strain; ε^0 and the corresponding variation.

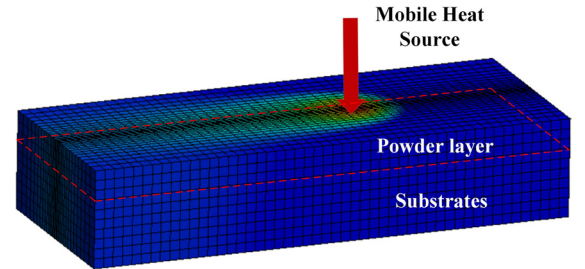


Figure 3. Calibration model of melt pool size.

Table 1. Parameters of the LPBF process.

Laser power(W)	Scan speed(mm/s)	Scan spacing(mm)	The thickness of powder spread(mm)	Laser beam diameter(mm)	Initial temperature(K)
200	800	0.12	0.04	0.15	298.15

The elastic strain in the free state is 0. Their thermal strain disappears when the metal parts are cooled to room temperature. The corresponding variable calculation can be neglected. Then the inherent strain ε^I is:

$$\varepsilon^I = \varepsilon^P \quad (8)$$

LPBF is a 3D printing process in which metal powder is fused by laser, creating a new object layer by layer. The interlayer interaction predicts stress and strains more complicated. There are significant errors in predicting the residual stress and deformation of parts directly according to the theory of initial inherent strain. Based on the improved inherent strain method²⁴⁻²⁶, intermediate state and steady state are defined. The elastic strain that is not completely released due to the evolution of mechanical boundary during deposition is considered. Two-layer deposition model is selected for LPBF thermo-mechanical coupling analysis. The intermediate state is defined as when the second layer of deposition has just been completed. The steady state is the time when the whole system temperature cools down to the ambient temperature. The improved inherent strain is calculated as follows:

$$\varepsilon^{In} = \varepsilon_{t_1}^{Plastic} + \varepsilon_{t_1}^{Elastic} - \varepsilon_{t_2}^{Elastic} = \varepsilon_{t_1}^{Total} - \varepsilon_{t_2}^{Elastic} \quad (9)$$

Where: ε^{In} is the improved inherent strain; $\varepsilon_{t_1}^{Plastic}$, $\varepsilon_{t_1}^{Elastic}$, and $\varepsilon_{t_1}^{Total}$ are the intermediate state plastic strain, elastic strain, and total strain, respectively; $\varepsilon_{t_2}^{Elastic}$ is the elastic strain at steady state.

The critical aspect of the inherent strain method is to extract representative inherent strain results. The implementation of the inherent strain method usually establishes a small-scale thermo-mechanical coupling model to obtain deformation

results. The small-scale model generally chooses two deposition layers to represent the local model of the actual laser deposition path. The model of two deposition layers can fully reflect the influence of the deposition process inter-layer remelting, inter-layer remelting, inter-layer binding force, and other factors on the deformation. In the two-layer deposition layer model, the nodes on the top surface of the first layer are selected to extract the inherent strain. Because the points on the top surface of the first layer all experience melting and remelting as well as interlayer restraint forces during the LPBF process.

A thermo-mechanical coupling model of LPBF double-layer deposition is established to extract the inherent strain. When simulating the LPBF double-layer deposition model, the scanning mode is shown in Figure 4. The scanning directions of the upper and lower layers are perpendicular to simulate the commonly used bidirectional alternating serpentine scanning mode. The double sediment layer size is 0.6mm×0.6mm×0.08mm, the mesh size is 0.002mm×0.02 mm×0.01mm, the substrate size is 1.0mm×1.0mm×0.2mm, the mesh size is 0.04mm×0.04mm×0.04mm. There are 56269 nodes and 12200 elements in total, and the lower surface of the substrate is fixed.

In thermal analysis, the element birth and death technique is used to simulate the accumulation process of the material with the heat source during LPBF. All the elements in the deposited layer are killed before the heat source starts to move. When the heat source starts to move, the elements at the current heat source are activated. After forming, set 5s cooling time to reach room temperature. The strain results in the intermediate state and steady state are obtained, and four analysis paths are created on the upper surface of the first layer of the deposition layer, as shown in Figure 4. According to the Formula 9 of the improved inherent strain method, the

Table 2. Mechanical properties of Ti-6Al-4V^{33,34}.

Parameters	Value					
	300	500	700	900	1100	1300
Temperature (K)	300	500	700	900	1100	1300
Elastic modulus (GPa)	122.7	110.5	97.4	60.8	24.3	0.2
Plastic tangent modulus (GPa)	2.7	2.6	2.0	0.4	0.02	0.01
Thermal expansion coefficient (10 ⁻⁶ /K)	8.9	9.9	10.8	11.4	11.6	11.9
Yield strength (MPa)	995.5	713.6	538.6	348.1	32.5	6.2
Poisson ratio	0.33	0.35	0.36	0.37	0.39	0.44

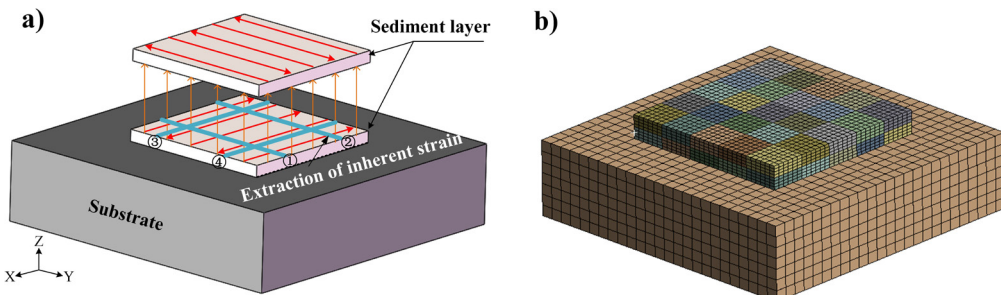


Figure 4. Thermo-mechanical Coupling Model of LPBF Double Layer Deposition (a) scanning method (b) meshing finite element model.

average strain values of x , y , and z directions are extracted from the four paths shown in Figure 4 as the inherent strain.

The LPBF forming process is a layer-by-layer stacking process. The element birth and death technique is used to activate layer by layer, and the inherent strain is loaded by the thermal strain method. The extracted inherent values are converted into the orthotropic thermal expansion coefficients to impose different thermal strains on the element. Realize the shrinkage of materials in different directions, and simulate the shrinkage process in thermal deformation. The conversion method of the expansion coefficient is as follows:

$$\alpha = \varepsilon^{In} / \Delta T \quad (10)$$

Where: α is the coefficient of thermal expansion; ε^{In} is the inherent strain value; ΔT is the temperature change, which is taken as -1 K. The coefficient of expansion obtained from Equation 10 is used as a material parameter to calculate the original material's thermal expansion coefficient.

Since LPBF technology is laser sintering forming of metal powder, it is limited by the size of the metal powder and equipment. According to the conclusions presented in the literature^{7,35-38} for the study of the forming process characteristics of the lattice structures, the Table 3 lattice cell size constraints were applied.

In this section, the average inherent strain calculated by thermo-mechanical coupling simulation is loaded into the lattice structures simulation as an input. The residual deformation and stress of lattice structures during LPBF forming were studied. Taking the BCC lattice as an example, the lattice configuration constraint consists of $3 \times 3 \times 3$ BCC lattice cells with the dimensional configuration shown in Figure 5, whose cell diameter $d=0.5$ mm, rod length $l=4$ mm, and rod inclination angle $\theta=45^\circ$.

The mesh is divided by the Cartesian method, and the individual size of the voxel is set to 0.08mm. In the simulation, layer-by-layer printing and forming can be realized by applying the element birth and death technique function. In the beginning, all model units are activated layer by layer. Under the action of inherent strain, each layer activation will produce deformation and stress. When all layers are activated, the accumulated deformation is the final deformation of the part.

3. Results and Discussion

3.1. Calibration results

The contour line of the melting pool was measured as shown in Figure 6. The observed width and depth of the melting pool were 133.42 and 61.59 μm , respectively. The simulating error is up to 34.4% without considering the thermal conductivity enhancement factor.

The anisotropic thermal conductivity enhancement coefficients $\omega_x=3$, $\omega_y=3$, and $\omega_z=9$ were chosen for group 5. The simulated predicted melt pool width and depth values were 132.98 μm and 63.36 μm with errors of 0.3% and 2.9%, respectively. By controlling the thermal conductivity enhancement coefficients in each direction (as shown in Table 4), the average errors in the melt pool depth and width directions were reduced to less than 2%.

Calculating the average inherent strain according to Formula 9 $\varepsilon_x=-0.00497$, $\varepsilon_y=-0.00497$, $\varepsilon_z=-0.0169$. Converting to anisotropic thermal expansion coefficient according to Formula 10 $\alpha_x=0.00497$, $\alpha_y=0.00497$, $\alpha_z=0.0169$. Change the material parameters to calculate the deformation results of structural members.

To verify the accuracy of the results, the inherent strain method was used to simulate the LPBF double-layer

Table 3. Size constraints of lattice cell.

Molding angle $\theta/^\circ$	Without support angle $\theta/^\circ$	Rod diameter d/mm	Rod length l/mm	Aspect Ratio l/d
≥ 20	≥ 43	≥ 0.3	≤ 5	4.39~22.9

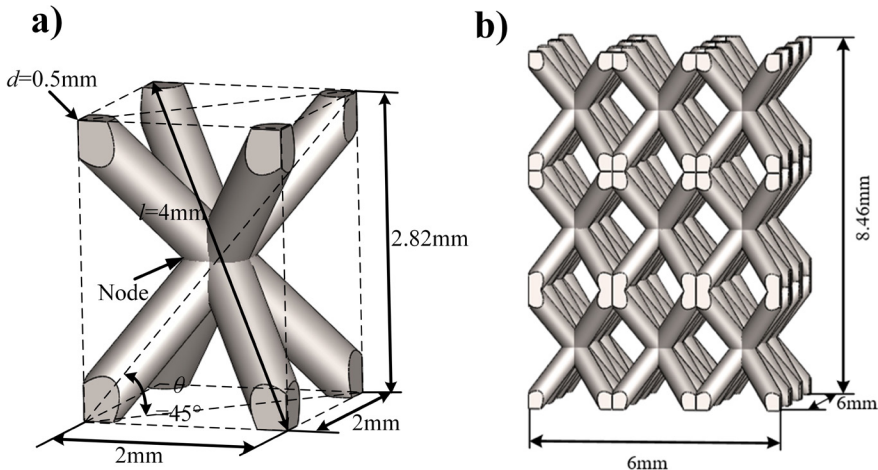


Figure 5. (a) Schematic diagram of the dimensions of a lattice cell (b) Schematic diagram of the dimensions of multilayer BCC lattice structure.

deposition model. The residual deformation and stress results are compared with the steady state results of the thermo-mechanical coupling method.

The maximum residual deformation of the thermo-mechanical coupled simulation is $2.41\ \mu\text{m}$, and the maximum residual deformation of the inherent strain method simulation result is $2.23\ \mu\text{m}$, where the relative error is 7.73%. Extract the deformation amount of each node on the centerline and sideline of the contact surface between the deposition layer and the substrate for comparison, as shown in Figure 7. The deformation trends of the two methods are consistent on the nodes of the centerline and sideline. The average error of the total deformation simulated by the inherent strain method on the centerline relative to the thermomechanical coupling results is 4.28%. The average error of the total deformation on the sideline is 11.4%.

The residual stresses on the centerline of the double-layer deposition model at different heights along the z-direction

as shown in Figure 8a were extracted for analysis. It can be seen from Figure 8b that the residual stress distribution trend simulated by the inherent strain method and the thermo-mechanical coupled method is the same. The value of residual stress in the double-layer deposition model decreases along the z-direction. The residual stress at the bottom of the sediment layer is mainly concentrated in the outer part, and the residual stresses at the top are mainly concentrated in the middle. However, the inherent strain method predicts slightly larger values of residual stresses than the thermo-mechanical coupled model. The reason is that the inherent strain method does not consider such factors as material properties that vary with temperature³⁵. In addition, the same model's inherent strain method takes 3 minutes to simulate compared to 40 minutes for the thermo-mechanical coupled model. The calculation time of the inherent strain method is reduced by 92% compared to the thermo-mechanical coupled method.

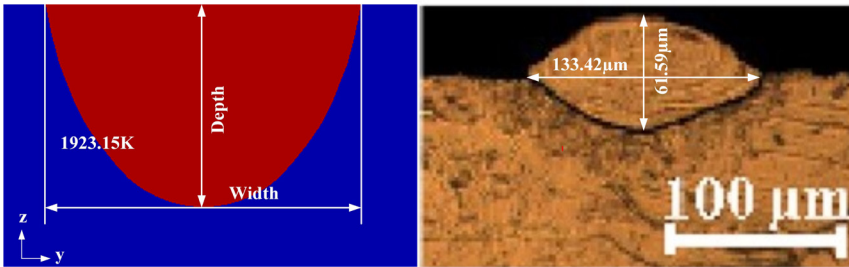


Figure 6. Comparison of simulated and experimental melt pools²⁶.

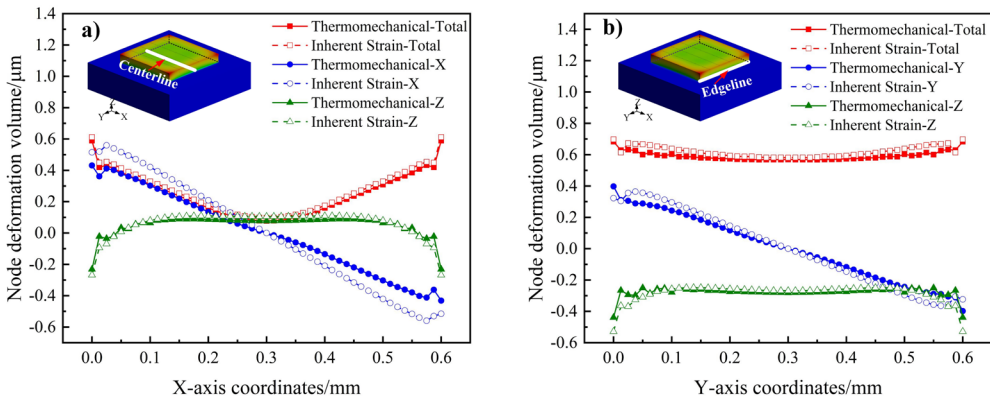


Figure 7. (a) Comparison of center line node deformation (b) Comparison of edge line node deformation.

Table 4. Anisotropic thermal conductivity enhancement factor.

Model No.	w_x	w_y	w_z	Melt pool width/ μm	Melt pool depth/ μm	Width error/%	Depth error/%	Average error/%
1	1	1	1	179.24	49.98	34.3	18.8	26.6
2	1	1	2	163.22	61.68	22.3	0.14	11.2
3	1	1	3	152.42	65.69	14.2	6.6	10.4
4	2	2	6	143.11	68.02	7.3	10.4	8.9
5	3	3	9	132.98	63.36	0.3	2.9	1.6

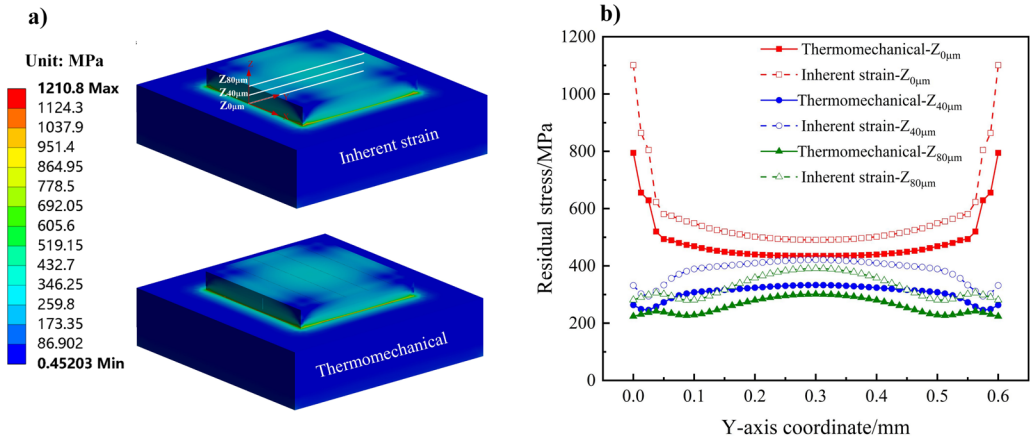


Figure 8. (a) Residual stress of LPBF double-layer deposition model under two methods (b) Residual stress at different heights along the Z direction.

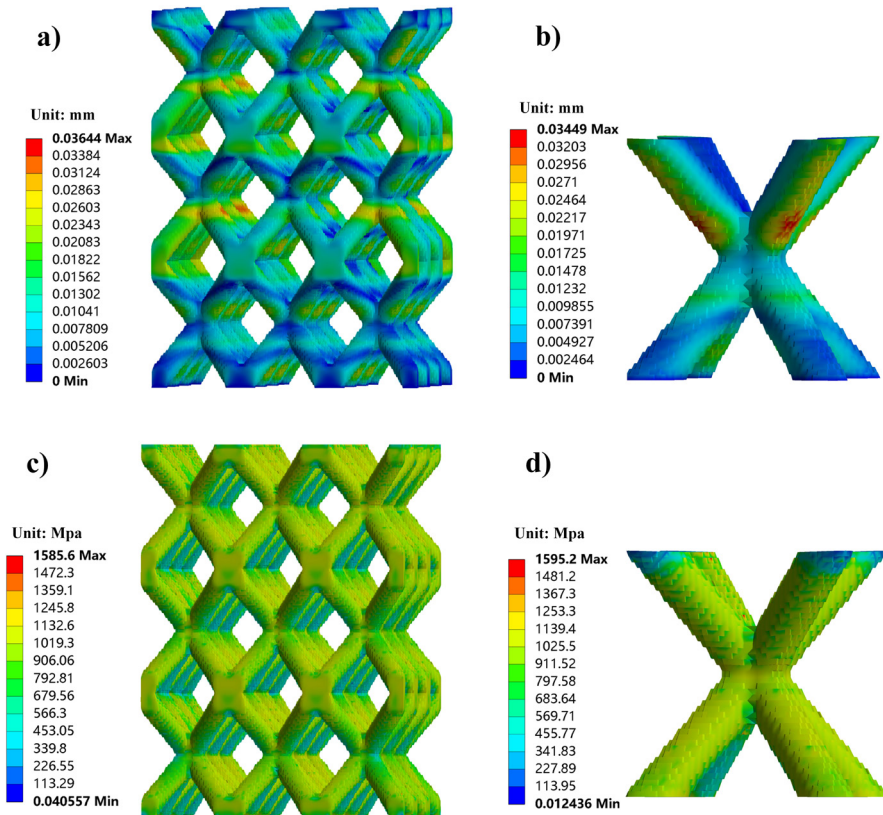


Figure 9. Residual deformation and stress results of LPBF manufacturing lattice structures (a) Residual deformation of multilayer BCC lattice structure (b) Residual deformation of BCC lattice cell (c) Residual stress of multilayer BCC lattice structure (d) Residual stress of BCC lattice cell.

3.2. Deformation and stress results

The residual deformation and stress clouds of the BCC lattice structure after printing are shown in Figure 9. The figure shows that the outer contour of the lattice structure is stepped, which is different from the actual forming surface. This is due to the limited computing

power of the computer. After reasonable treatment of the actual powder layer thickness in the simulation process, the computer magnified the actual structure due to the layered stacking effect. The residual deformation of the BCC lattice structure is mainly concentrated on one side of the lower surface of the inclined rod. The closer to the node, the smaller the residual deformation, and the more

horizontal the residual deformation distribution. This is due to the high temperature of the melt pool at the overhanging position and the large temperature gradient, which makes it easy to have significant thermal stresses.

The residual deformation and stress distribution clouds of a single lattice cell in multilayer lattice structures are shown in Figure 9b-9d in separate simulations. The residual deformation and stress distribution trends of a single lattice cell are the same as those of a single cell in the center of multilayer lattice structures. Meanwhile, the maximum residual deformation was 0.0345 mm and 0.0345 mm for a single lattice cell and multilayer lattice structures, and the maximum residual deformation was 1595 MPa and 1585 MPa, respectively. The residual deformation and residual stress of multilayer lattice structures and a lattice cell are similar in value. Therefore, it can be considered that a single lattice cell individual is the smallest unit that determines the residual deformation and stress of the multilayer lattice structures. So when exploring the effect of the lattice structure's geometry factors on residual deformation and stress, it is possible to use only a single lattice cell as an example for calculation.

Table 5. Simulation parameter settings.

No.	Rod inclination $\theta/^\circ$	Rod diameter d/mm	Rod length l/mm
1	15~75($\Delta\theta=5$)	0.5	4
2	45°	0.2~1.1($\Delta d=0.1$)	4
3	45°	0.5	2~11($\Delta l=1$)

3.3. Influencing factors analysis

Three numerical simulation cases are set as shown in Table 5. Taking the BCC lattice cell as an example, the effects of geometric factors, such as rod inclination, rod diameter, and rod length, on residual deformation and stress are discussed. The maximum residual deformation and stress of the whole BCC lattice cell, bottom surface, node surface, and top surface are extracted for analysis.

Figure 10 shows the variation trend of the maximum residual deformation and stress of the whole BCC lattice cell and different parts with the inclination, diameter, and length of the rod.

As shown in Figure 10a, with the same rod diameter and length, the maximum residual deformation decreases sharply from 15° to 40° with increased rod inclination and then gradually becomes smooth. It can also be seen that the deformation trend of the top surface is the same as that of the whole, and the bottom surface is the same as that of the node surface. In addition, the residual deformation distribution becomes more and more uniform with the increase of the rod inclination angle, as can be seen from the cloud diagram. This is because the deformation of the inclined rod in the BCC lattice cell is mainly caused by warpage and shrinkage³⁹. When the inclination angle of the rod is less than 40°, the deformation is primarily driven by warping. And when the inclination angle of the rod is greater than 40°, the deformation is mainly caused by shrinkage. This is due to the fact that when the rod inclination is less than 40°, the smaller the rod inclination is, the shorter the overlap length between layers is, and the corresponding overhang length increases. While the powder support length of the forming layer increases and the laser spot will shine

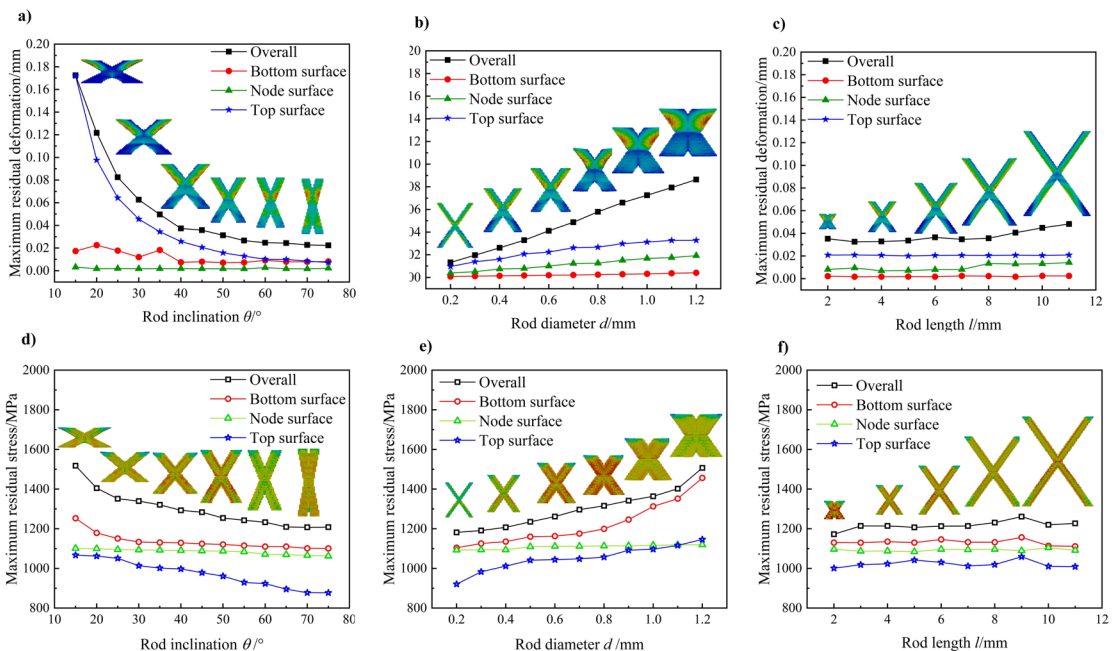


Figure 10. (a) Variation of maximum residual deformation with rod inclination (b) Variation of maximum residual deformation with rod diameter (c) Variation of maximum residual deformation with rod length (d) Variation of maximum residual stress with rod inclination (e) Variation of maximum residual stress with rod diameter (f) Variation of maximum residual stress with rod length.

more on the powder support area. However, the poor heat dissipation of the powder leads to the formation of a large melt pool, which generates a large temperature gradient and leads to warping deformation near the overhanging surface. Furthermore, the powder support length gradually decreases in the rod inclination angle greater than 40°. At this time, the powder mainly causes deformation in the role of laser melting and solidification shrinkage. On the other hand, the cooling rate of inclined struts was higher than that of vertical struts in LPBF forming technology⁴⁰, which was another reason why the residual deformation decreased with the increase of rod inclination.

The maximum residual deformation of the BCC lattice cell with different rod diameters is shown in Figure 10b. From the figure, it can be concluded that the maximum residual deformation of a BCC lattice cell increases linearly with the increase in rod diameter. Moreover, the maximum residual deformation changes from the bottom to the top surface with the same trend and increases with the height increase. The reason for this is that the overlapping area between the formed powder layers increases with increasing rod diameter at the same rod inclination. Subsequently, the laser action time and area will also increase. The larger the forming area is, the larger the corresponding shrinkage is, and the relationship is linear.

Figure 10c simulates the variation of the maximum residual deformation of the BCC lattice cell with the rod length. It is not difficult to conclude that the maximum residual deformation of the lattice cell increases slowly with the rod length, and the rod length has no significant effect on the residual deformation. Since the residual deformation of the lattice structure is more affected by the constraint of the substrate when the rod length is short. At this time, the whole structure is closer to the substrate, heat dissipation is better, and residual deformation increases slowly. While, with the increase of the rod length, the substrate's constraint on the lattice structure gradually decreases. At the same time, the heat dissipation environment tends to be stable and the deformation also tends to be stable.

Figure 10d-10f show the effects of different lattice geometry parameters on the maximum residual stresses in the BCC lattice. Compared with Figure 10a-10c, it can be found that the effect of lattice geometry parameters on the residual stress is similar to the effect on the residual deformation. However, the influence of geometric parameters on residual stress is not as apparent as that on residual deformation. The maximum residual stress decreases with increasing rod inclination and increases with increasing rod diameter, and the rod length has almost no effect on the residual stress. Furthermore, for different geometrical parameters, the maximum residual stresses in the BCC lattice cells decrease sequentially from the bottom to the nodes to the top, contrary to the residual deformation pattern.

4. Conclusions

1. The accuracy of the thermo-mechanical coupling model was improved by adding anisotropic thermal conductivity enhancement coefficients. In verifying the accuracy of the inherent strain method, the average error of the inherent strain method relative to the

thermomechanical coupling method is about 7%. According to the error analysis results, the results of simulating the residual deformation and stress of the lattice using the inherent strain method are referable. In addition, the inherent strain method is used to significantly shorten the calculation time.

2. Compared with the results of residual deformation and stress of lattice forming, a lattice cell's residual deformation and stress distribution is the same as that of the cell in the center of the multilayer lattice. The maximum residual deformation and stress are similar in value. A lattice cell can be regarded as the smallest element that determines the residual deformation and stress of the lattice structures.
3. When the angle of the lattice cell rod is less than 40°, the influence of the angle on the maximum residual deformation is more significant. When the angle is greater than 40°, the effect of the angle on the minimum residual deformation is rapidly weakened. The maximum residual deformation of lattice cells increases linearly with the increase in rod diameter. The influence of rod length on its residual deformation can be ignored. Under different geometric parameters, the maximum residual deformation of BCC lattice cells increases with the height from the bottom to the node surface to the top.
4. The maximum residual stress decreases slowly with the increase of the rod angle and increases gently with the rise of the rod diameter. The length of the rod has little effect on the residual stress. With different geometric parameters, the maximum residual stress of the BCC lattice cell decreases with the height from the bottom to the node surface to the top.
5. Since it is difficult to remove supports from the lattice structures in actual printing, this work focuses on the effect of residual deformation and stresses generated during the unsupported forming of the lattice structures. However, in practice use, LPBF printed parts mainly use dense components and supports for heat dissipation to reduce thermal stress. The effect of supports on residual deformation and stresses is impossible to be ignored. Therefore, further research is needed to investigate the effect of support on residual stress and deformation. In addition, this work lacks experimental verification of residual deformation and stresses in the lattice structures, which is hoped to be further improved in future work.

5. Acknowledgements

This work was supported by the National Natural Science Foundation of China [grant number 12102016] and the Natural Science Foundation of Beijing Municipality [grant number 3202001].

6. Reference

1. Pan C, Han Y, Lu J. Design and optimization of lattice structures: a review. *Appl Sci.* 2020;10:6374.
2. Korshunova N, Alaimo G, Hosseini SB, Carraturo M, Reali A, Niiranen J et al. Image-based numerical characterization

- and experimental validation of tensile behavior of octet-truss lattice structures. *Addit Manuf.* 2021;41:101949.
3. Liao G, Luan C, Wang Z, Liu J, Yao X, Fu J. Acoustic metamaterials: a review of theories, structures, fabrication approaches, and applications. *Adv Mater Technol.* 2021;6:2000787.
 4. Guddati S, Kiran ASK, Leavy M, Ramakrishna S. Recent advancements in additive manufacturing technologies for porous material applications. *Int J Adv Manuf Technol.* 2019;105:193-215.
 5. Nazir A, Abate KM, Kumar A, Jeng JY. A state-of-the-art review on types, design, optimization, and additive manufacturing of cellular structures. *Int J Adv Manuf Technol.* 2019;104:3489-510.
 6. Plessis A, Broeckhoven C, Yadroitsava I, Yadroitsev I, Hands CH, Kunju R et al. Beautiful and functional: a review of biomimetic design in additive manufacturing. *Addit Manuf.* 2019;27:408-27.
 7. Zhang XZ, Tang HP, Leary M, Song T, Jia L, Qian M. Toward manufacturing quality Ti-6Al-4V lattice struts by Selective Electron Beam Melting (SEBM) for lattice design. *JOM.* 2018;70:1870-6.
 8. Kadirgama K, Harun WSW, Tarlochan F, Samykano M, Ramasamy D, Azir MZ et al. Statistical and optimize of lattice structures with selective laser melting (SLM) of Ti6AL4V material. *Int J Adv Manuf Technol.* 2018;97(1-4):495-510.
 9. Xiao Z, Yang Y, Xiao R, Bai Y, Song C, Wang D. Evaluation of topology-optimized lattice structures manufactured via selective laser melting. *Mater Des.* 2018;143:27-37.
 10. Plocher J, Panesar A. Review on design and structural optimisation in additive manufacturing: towards next-generation lightweight structures. *Mater Des.* 2019;183:108164.
 11. Zhang K, Qu H, Guan H, Zhang J, Zhang X, Xie X et al. Design and fabrication technology of metal mirrors based on additive manufacturing: a review. *Appl Sci.* 2021;11:10630.
 12. DebRoy T, Wei HL, Zuback JS, Mukherjee T, Elmer JW, Milewski JO et al. Additive manufacturing of metallic components – process, structure, and properties. *Prog Mater Sci.* 2018;92:112-224.
 13. Moreno DM No, Moreno DS. Design for additive manufacturing: tool review and a case study. *Appl Sci.* 2021;11:1571.
 14. Maconachie T, Leary M, Lozanovski B, Zhang X, Qian M, Faruque O et al. SLM lattice structures: properties, performance, applications, and challenges. *Mater Des.* 2019;183:108137.
 15. Alomar Z, Concli F. A review of the selective laser melting lattice structures and their numerical models. *Adv Eng Mater.* 2020;22:2000611.
 16. Jia H, Sun H, Wang H, Wu Y, Wang H. Scanning strategy in selective laser melting (SLM): a review. *Int J Adv Manuf Technol.* 2021;113:2413-35.
 17. Razavykia A, Brusa E, Delprete C, Yavari R. An overview of additive manufacturing technologies: a review to technical synthesis in numerical study of selective laser melting. *Materials.* 2020;13:3898.
 18. Zhou R, Liu H, Wang H. Modeling and simulation of metal selective laser melting process: a critical review. *Int J Adv Manuf Technol.* 2022;121:5693-706.
 19. Ueda Y, Fukuda K, Nakacho K, Endo S. A new measuring method of residual stresses with the aid of finite element method and reliability of estimated values. *J Soc Nav Architects Jpn.* 1975;1975:499-507.
 20. Deng D, Murakawa H, Liang W. Numerical simulation of welding distortion in large structures. *Comput Methods Appl Mech Eng.* 2007;196:4613-27.
 21. Keller N, Ploshikhin V. New method for fast predictions of residual stress and distortion of AM parts. In: *International Solid Freeform Fabrication Symposium; 2014 Aug 4-6; Austin. Proceedings. Austin: The University of Texas at Austin; 2014. p. 1229-37.*
 22. Siewert M, Neugebauer F, Epp J, Ploshikhin V. Validation of mechanical layer equivalent method for simulation of residual stresses in additive manufactured components. *Comput Math Appl.* 2019;78:2407-16.
 23. Setien I, Chiumenti M, van der Veen S, Sebastian MS, Garcíandía F, Echeverría A. Empirical methodology to determine inherent strains in additive manufacturing. *Comput Math Appl.* 2019;78:2282-95.
 24. Liang X, Cheng L, Chen Q, Yang Q, To AC. A modified method for estimating inherent strains from detailed process simulation for fast residual distortion prediction of single-walled structures fabricated by directed energy deposition. *Addit Manuf.* 2018;23:471-86.
 25. Liang X, Chen Q, Cheng L, Hayduke D, To AC. Modified inherent strain method for efficient prediction of residual deformation in direct metal laser sintered components. *Comput Mech.* 2019;64:1719-33.
 26. Liang X, Dong W, Hinnebusch S, Chen Q, Tran HT, Lemon J et al. Inherent strain homogenization for fast residual deformation simulation of thin-walled lattice support structures built by laser powder bed fusion additive manufacturing. *Addit Manuf.* 2020;32:101091.
 27. Chen Q, Liang X, Hayduke D, Liu J, Cheng L, Oskan J et al. An inherent strain based multiscale modeling framework for simulating part-scale residual deformation for direct metal laser sintering. *Addit Manuf.* 2019;28:406-18.
 28. Dong W, Liang X, Chen Q, Hinnebusch S, Zhou Z, To AC. A new procedure for implementing the modified inherent strain method with improved accuracy in predicting both residual stress and deformation for laser powder bed fusion. *Addit Manuf.* 2021;47:102345.
 29. Kamara AM, Wang W, Marimuthu S, Li L. Modelling of the melt pool geometry in the laser deposition of nickel alloys using the anisotropic enhanced thermal conductivity approach. *Proc Inst Mech Eng, B J Eng Manuf.* 2011;225:87-99.
 30. Yin J, Zhu H, Ke L, Hu P, He C, Zhang H et al. A finite element model of thermal evolution in laser micro sintering. *Int J Adv Manuf Technol.* 2016;83:1847-59.
 31. Yin J, Peng G, Chen C, Yang J, Zhu H, Ke L et al. Thermal behavior and grain growth orientation during selective laser melting of Ti-6Al-4V alloy. *J Mater Process Technol.* 2018;260:57-65.
 32. Mills KC. Recommended values of thermophysical properties for selected commercial alloys. Cambridge: Woodhead Publishing; 2002. *Ti: Ti-6 Al-4 V (IMI 318); p. 211-7.*
 33. Rangaswamy P, Prime MB, Daymond M, Bourke MAM, Clausen B, Choo H et al. Comparison of residual strains measured by X-ray and neutron diffraction in a titanium (Ti-6Al-4V) matrix composite. *Mater Sci Eng A.* 1999;259:209-19.
 34. Vanderhastan M, Rabet L, Verlinden B. Ti-6Al-4V: deformation map and modelisation of tensile behaviour. *Mater Des.* 2008;29:1090-8.
 35. Rehme O, Emmelmann C. Rapid manufacturing of lattice structures with selective laser melting. In: *Proceedings of SPIE - The International Society for Optical Engineering; 2006 Jan 21-26; San Jose. Proceedings. Bellingham: SPIE; 2006. p. 192-203.*
 36. Buchbinder D, Schleifenbaum H, Heidrich S, Meiners W, Bültmann J. High power selective laser melting (HP SLM) of aluminum parts. *Phys Procedia.* 2011;12:271-8.
 37. Yan C, Hao L, Hussein A, Young P, Raymont D. Advanced lightweight 316L stainless steel cellular lattice structures fabricated via selective laser melting. *Mater Des.* 2014;55:533-41.
 38. Mazur M, Leary M, Sun S, Vcelka M, Shidid D, Brandt M. Deformation and failure behaviour of Ti-6Al-4V lattice structures manufactured by selective laser melting (SLM). *Int J Adv Manuf Technol.* 2016;84:1391-411.
 39. Ilin A, Logvinov R, Kulikov A, Prihodovsky A, Xu H, Ploshikhin V et al. Computer aided optimisation of the thermal management during laser beam melting process. *Phys Procedia.* 2014;56:390-9.
 40. Xie Z, Dai Y, Ou X, Ni S, Song M. Effects of selective laser melting build orientations on the microstructure and tensile performance of Ti-6Al-4V alloy. *Mater Sci Eng A.* 2020;776:139001.